Journal of the European Ceramic Society 22 (2002) 1609–1620

www.elsevier.com/locate/jeurceramsoc

Phase and microstructural evolution during the heat treatment of Sm–Ca–α-sialon ceramics

A.J. Seeber[a,*], Y.-B. Cheng[a], I. Harrowfield[b]

[a]*School of Physics and Materials Engineering, Monash University, Victoria 3800, Australia*
[b]*Minerals Division, CSIRO, Normandy Road Clayton, Victoria 3168, Australia*

Received 10 April 2001; received in revised form 1 October 2001; accepted 13 October 2001

Abstract

The phase and microstructural evolution of multi-cation Sm–Ca–α-sialon ceramics was investigated. Six samples were prepared, ranging from a pure Sm-sialon to a pure Ca-sialon, with calcium replacing samarium in 20 eq% increments, thus maintaining an equivalent design composition in all samples. After pressureless sintering at 1820 °C for 2 h, all samples were subsequently heat treated up to 192 h at 1450 and 1300 °C. The amount of grain boundary glass in the samples after sintering was observed to decrease with increasing calcium levels. A M'_{ss} or M'_{ss}-gehlenite solid solution was observed to form during the 1450 °C heat treatment of all Sm-containing samples, and this phase forms in clusters in the high-Sm samples. The thermal stability of the α-sialon phase was improved in the multi-cation systems. Heat treatment at 1300 °C produces $SmAlO_3$ in the high-Sm samples, a M'_{ss}-gehlenite solid solution in the high-Ca samples, and a Sm–Ca–apatite phase in some intermediate samples.

Keywords: Microstructure-final; Phase development; Sialon; X-ray methods

1. Introduction

The α-sialon (α′) phase is a solid solution of α-Si_3N_4, and can be represented by the general formula $M_{m/v}Si_{12-(m+n)}Al_{(m+n)}O_nN_{16-n}$, where M is a metal cation (lithium, magnesium, calcium and most rare-earth elements), v is the valency of that metal cation, m is the number of Si–N bonds replaced by Al–N bonds, and n is the number of Si–N bonds replaced by Al-O bonds.[1] The symbol 'x' is also commonly used to denote total quantity of α′-stabilising cation, in place of m/v in the α-sialon formula. Sialon ceramics hold several advantages over Si_3N_4, in that properly chosen sintering additives may be incorporated within the sialon crystal structure, reducing the amount of residual grain boundary phase.[2] The α′ phase also has the advantage of improved hardness relative to the β-sialon phase (β′, isostructural with β-Si_3N_4). Although the fracture toughness of α′-based ceramics is generally thought inferior to that of β′-based materials, the recent discovery of α′-based materials with improved fracture toughness through nucleation control[3,4] seems to indicate that this problem may be overcome.

However, the thermal stability of the α′ phase is another issue of concern. Post-sintering heat treatment is generally used to devitrify residual grain boundary glass to a refractory crystalline phase, in order to improve the performance of the material at high temperatures. It has been found that the α′ phase may transform to the β′ phase during this heat treatment,[5] resulting in a decline in mechanical properties over time. A number of comparative studies on this phenomena have been undertaken,[5–9] which indicate that α′ phase stability decreases with increasing rare earth cation radius/decreasing rare earth atomic number. As with the α→β Si_3N_4 phase transformation,[10] the presence of seeds of the β′ phase after sintering is required in order to facilitate the α′→β′ phase transformation. While less research has been undertaken on calcium-based α-sialon systems, research thus far seems to indicate that Ca-α′ phase stability is quite high,[11] and may not be affected by the presence of prior β′ seeds as much as rare-earth-stabilised α′-based materials.[12] However, the grain boundary phases are expected to be less refractory in the Ca–Si–Al–O–N system than in the rare-earth-based

* Corresponding author.
E-mail address: aaron.seeber@spme.monash.edu.au (A.J. Seeber).

0955-2219/02/$ - see front matter
PII: S0955-2219(01)00482-4

systems, such as the refractory M'_{ss} phase which may be produced on heat treatment of a samarium-based sialon.[13]

Sialon systems containing multiple α′-stabilising cations have also been studied. It has been demonstrated that rare earth cations which are difficult to incorporate within the α′ phase,[14] or otherwise insoluble may be incorporated within the α′ phase when accompanied with another, more soluble cation.[15,16] Multication systems have also been prepared where the β′ phase is not present, and, therefore, contain α′ phases that are resistant to transformation on heat treatment.[16–18] This study details the investigation of α′-rich Sm–Ca–sialon systems.

2. Experimental procedures

A series of samples in the Sm–Ca-sialon system was produced, based on the composition $m = 1.194$, $n = 1.614$ in the general α-sialon formula, which placed the composition near the edge of the α′-phase forming region. Calcium was incorporated to replace samarium on an equivalence basis to conserve the m-value. The design composition is shown as projected onto the Sm–α-sialon plane in Fig. 1, and the formulae and equivalent percentage of calcium-substitution-for-samarium in the various samples are shown in Table 1. The starting powders used were Si_3N_4 (H.C. Starck grade LC10, 1.94 wt.% oxygen), AlN (H.C. Starck grade B, 2 wt.% oxygen), Al_2O_3 (Ajax 'Labchem'), Sm_2O_3 (Heraeus 99.9%), and $CaCO_3$ (Ajax 99%). Surface oxides on the nitride powders were taken into account when formulating the mixtures, in accordance with the powder specifications provided by the manufacturers. The calcium carbonate powder was air-dried at 200 °C for 48 h then transferred to a desiccator, to remove absorbed water before use. Fifty gram batches of each sample were weighed out, to within 0.001 g. Powders were milled using Si_3N_4 balls in isopropanol for a period of 24 h, after which the isopropanol was dried off. Powders were then re-mixed by hand for 10 min in an agate mortar and pestle to further homogenise the powder mixture. The powders were uniaxially pressed into 2.5 cm diameter pellets, and subsequently cold isostatically pressed at 200 MPa. Pellet weight was approximately 10 g.

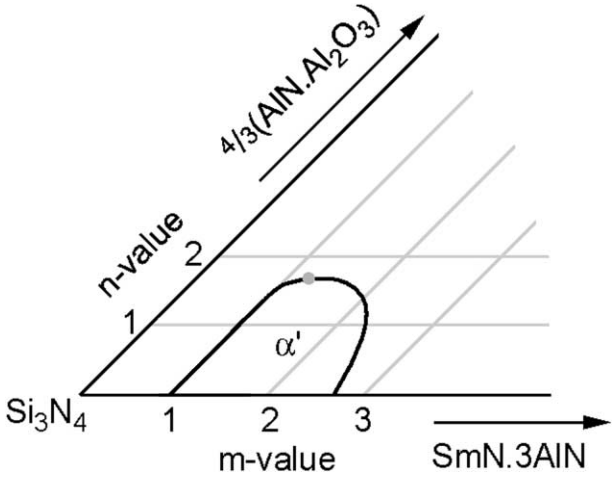

Fig. 1. The design composition as projected onto the Sm α-sialon plane.

Table 1
The formulae and equivalent % calcium-substitution-for-samarium for all samples

Sample	Formula	Eq% Ca
Sm10	$Sm_{0.412}Si_{9.512}Al_{2.906}O_{1.670}N_{14\cdot887}$	0
S8C2	$Sm_{0.329}Ca_{0.124}Si_{9.512}Al_{2.906}O_{1.670}N_{14\cdot887}$	20
S6C4	$Sm_{0.246}Ca_{0.248}Si_{9.512}Al_{2.906}O_{1.670}N_{14\cdot887}$	40
S4C6	$Sm_{0.164}Ca_{0.373}Si_{9.512}Al_{2.906}O_{1.670}N_{14\cdot887}$	60
S2C8	$Sm_{0.081}Ca_{0.497}Si_{9.512}Al_{2.906}O_{1.670}N_{14\cdot886}$	80
Ca10	$Ca_{0.618}Si_{9.512}Al_{2.906}O_{1.670}N_{14\cdot886}$	100

Samples were sintered in a graphite resistance furnace under a high purity nitrogen atmosphere. The firing schedule was as follows: 30 °C/min to 950 °C, hold $\frac{1}{2}$ h; 30 °C/min to 1500 °C, hold 1 h; 5 °C/min to 1820 °C, hold 2 h; then shut-off power. The natural cooling rate of this furnace ranged from ~50 °C/min at 1800 °C, decreasing to below 20 °C/min below 1000 °C, and taking a total of ~5 h to reach room temperature from the sintering temperature. A N_2 atmosphere was introduced above 950 °C, and below this temperature the samples were kept under vacuum to aid $CaCO_3$ decomposition, and also to remove CO_2 generated during the decomposition. After sintering, density was calculated using Archimedes principle.

Heat treatment of samples took place in an alumina tube furnace, again using a high purity nitrogen atmosphere. Heating rates used were 5 °C/min up to 800 °C, 3 °C/min above this temperature, with equivalent cooling rates. The sintered samples were heat treated at 1300 and 1450 °C, up to 192 h (8 days) at each temperature.

XRD analysis was performed with a Rigaku Geigerflex diffractometer using Ni-filtered Cu K_α radiation. The ratio of α′ to β′ was determined by the method of XRD peak mean-normalised-intensity of Gazzara and Messier[19] as developed by Li and O'Connor,[20] according to the formula:

$$V_{\beta'} = 1/\left(1 + I_{\alpha'} R_{\beta'} / I_{\beta'} R_{\alpha'}\right) \quad (1)$$

The intensity I of the (2 1 0) peaks for both the α′ and β′ phases were used, owing to their high intensity and low overlap with peaks from the other phases present. The normalising factors ($R_{\alpha'}$ and $R_{\beta'}$) for the (2 1 0) peak of these phases were calculated as being 8.40 and 11.76 respectively, using the program Volfract.[21]

Micrographs were obtained using a Jeol JSM 840A operating at 20 kV. Electron probe microanalysis (EPMA) was undertaken using a Jeol 8900R Superprobe equipped with wavelength dispersive spectrometers, operating at 15 kV. Wollastonite, spinel, BN, NdF_3 and pure Sm metal standards were used. The samples were carbon-coated prior to both examinations.

3. Results

3.1. XRD analyses of samples

Representative XRD spectra for selected samples are shown in Fig. 2. Table 2 shows all XRD results before and after heat treatment.

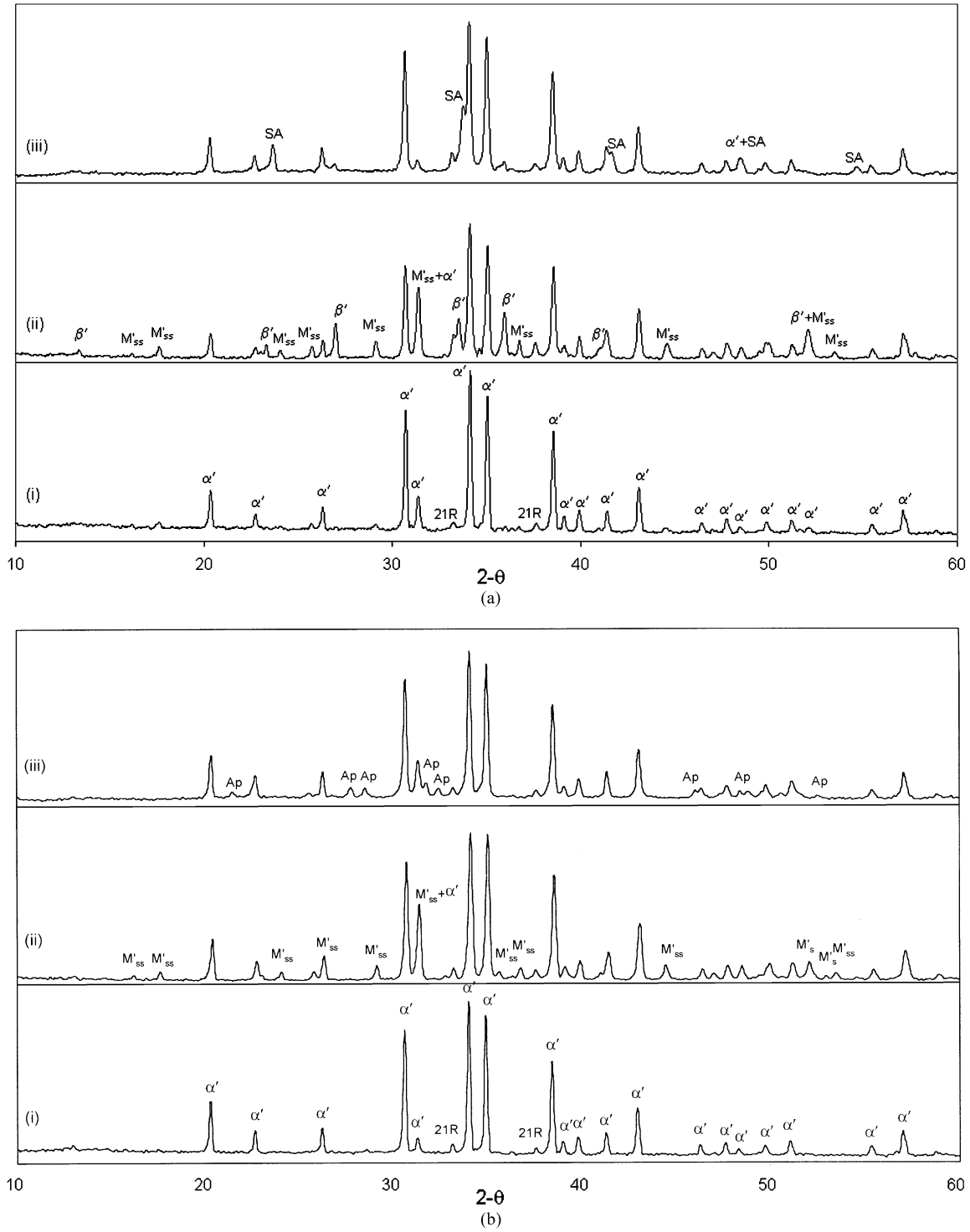

Fig. 2. XRD spectra for the (a) Sm10 sample and (b) S6C4 sample. In both cases the as fired (i), after 192 h heat treatment at 1450 °C (ii) and 192 h heat treatment at 1300 °C (iii) spectra are presented.

Table 2
XRD data for as-fired and heat-treated samples

Sample		As fired	24 h @1450 °C	96 h @1450 °C	192 h @1450 °C	24 h @1300 °C	96 h @1300 °C	192 h @1300 °C
Sm10	α′/β′ (wt.%)	98/2	95/5	87/13	77/23	98/2	97/3	96/4
	Other phases	21R (W)	21R (W)	21R (W)	21R (MW)	21R (W)	21R (W)	21R (MW)
		M'_{ss} (MW)	M'_{ss} (MW)	M'_{ss} (M)	M'_{ss} (M)	M'_{ss} (W)	M'_{ss} (VW)	SA (MW)
						SA[a] (W)	SA (MW)	
S8C2	α′/β′ (wt.%)	100/0	100/0	100/0	100/0	100/0	100/0	100/0
	Other phases	21R (W)	21R (W)	21R (W)	21R (W)	21R (W)	21R (W)	21R (W)
			M'_{ss} (W)	M'_{ss} (M)	M'_{ss} (M)	SA (W)	SA (W)	SA (VW)
						Ap[b] (W)	Ap (W)	Ap (W)
S6C4	α′/β′ (wt.%)	100/0	100/0	100/0	100/0	100/0	100/0	100/0
	Other phases	21R (W)	21R (W)	21R (W)	21R (VW)	21R (W)	21R (W)	21R (W)
			M'_{ss} (M)	M'_{ss} (M)	M'_{ss} (M)	SA (VW)	Ap (MW)	Ap (MW)
						Ap (W)		
S4C6	α′/β′ (wt.%)	100/0	100/0	100/0	100/0	100/0	100/0	100/0
	Other phases	21R (W)	21R (W)	21R (W)	21R (W)	21R (W)	21R (W)	21R (W)
			M'_{ss} (W)	M'_{ss} (W)	M'_{ss} (MW)	M'_{ss} (W)	M'_{ss} (W)	M'_{ss} (MW)
S2C8	α′/β′ (wt.%)	100/0	100/0	100/0	100/0	100/0	100/0	100/0
	Other phases	21R (W)	21R (W)	21R (W)	21R (W)	21R (W)	21R (W)	21R (W)
			M'_{ss} (W)	M'_{ss} (W)	M'_{ss} (W)	M'_{ss} (W)	M'_{ss} (W)	M'_{ss} (W)
Ca10	α′/β′ (wt.%)	100/0	100/0	100/0	100/0	100/0	100/0	100/0
	Other phases	21R (W)	21R (W)	21R (W)	21R (W)	21R (W)	21R (W)	21R (W)

X-ray intensities: W = weak, M = medium, V = very.
[a] SA = samarium aluminate: $SmAlO_3$.
[b] Ap = samarium-calcium-apatite phase: $Ca_2Sm_8(SiO_4)_6O_2$.

3.1.1. XRD analyses of the as-fired samples

According to the XRD spectra, α′ and 21R are the only crystalline phases found in all of these samples after firing. In all samples, α′ is the predominant phase. The pure-Sm-containing Sm10 sample is the only sample to contain either of the M'_{ss} and β′ phases on sintering, and small quantities of each—less than 2% β′ as a function of α′ and β′. This illustrates the effectiveness of calcium as an α′-forming cation, as the substitution of only a small amount of the samarium for calcium has impeded the formation of the β¢ phase at this sintering temperature.

3.1.2. XRD analyses of the samples after heat treatment at 1450 °C

Heat treatment at 1450 °C resulted in α′→β′ transformation only in the pure-Sm Sm10 sample. Even after 192 h heat treatment at 1450 °C, α′ is still the dominant phase, though M'_{ss} levels are observed to increase in this sample as the heat treatment progresses. Heat treatment has also resulted in the formation of a melilite-gehlenite-solid-solution phase (henceforth referred to as $(M'\text{-}G)_{ss}$) in all Ca-containing samples bar the pure-Ca sample, but α′ is still the dominant phase in all these samples even after 192 h heat treatment at 1450 °C.

The M'_{ss} XRD peak intensity is observed to decrease with increasing calcium levels, as seen in Table 2. This tendency towards smaller quantities of the grain boundary phase being observed with increasing calcium content may be explained in terms of the higher solubility of the calcium cation within the α′ phase as compared with samarium. However, it should also be noted that for XRD phase analysis, the $(M'\text{-}G)_{ss}$ phase structure factors would be expected to decrease with increasing calcium content. M'_{ss} and $(M'\text{-}G)_{ss}$ structure factors were not calculated due to extinction problems related to the expected large grain size of this phase.[22] Therefore, $(M'\text{-}G)_{ss}$ phase content was examined via image analysis, which will be detailed in Section 3.4. However, it can be hypothesised at this point that $(M'\text{-}G)_{ss}$ phase content decreases with increasing calcium content, as no gehlenite is observed in the pure-Ca Ca10 sample.

3.1.3. XRD analyses of the samples after heat treatment at 1300 °C

The α′→β′ transformation during heat treatment at 1300 °C is considerably slower than at 1450 °C. Once again, the decomposition only occurs in the pure-Sm Sm10 sample, but less than 5% β′ as a function of α′ and β′ is found after 192 hours heat treatment at 1300 °C, and the α′ phase in all Ca-containing samples was found not to decompose at all.

Heat treatment at 1300 °C resulted in the formation of $SmAlO_3$ in the high-Sm samples. While M'_{ss} had formed in the pure-Sm Sm10 sample during the sintering stage,

the amount of M'_{ss} is seen to decrease as the $SmAlO_3$ forms. This phenomena has been seen before, where unquenched (furnace cooled) sialon samples are observed to contain small quantities of M'_{ss} after sintering. This M'_{ss} has been seen to either reduce in intensity with aluminate formation on heat treatment around 1300 °C,[23] or even disappear altogether.[24] Since only a small amount of M'_{ss} is found after sintering, there is presumably still a large amount of glass present. This may be confirmed by observing the large increase in M'_{ss} XRD peak intensity in the pure-Sm Sm10 sample heat-treated at 1450 °C, accompanied by a lesser increase in β′ content, as shown in Fig. 2(a). This indicates that M'_{ss} formation must come from grain boundary devitrification as well as α′→β′ transformation.[25] $SmAlO_3$ has been observed to be the preferred grain boundary phase in Sm-based sialon ceramics under a 1300 °C heat treatment, as seen by the XRD results above, as well as in other studies.[13,23,24] Therefore, it is proposed that the residual M'_{ss} phase after sintering is not stable at the post-sintering heat treatment temperature of 1300 °C, and is slowly dissolved into the grain boundary glass. Upon solution, the aluminate phase may be precipitated on reaction of the grain boundary liquid with the α′ phase. This is interesting as it indicates that with Sm–M'_{ss}, as with other phases in this system, long-term stability is dependant on the temperature-and-time conditions to which the ceramic is subjected. The presence of a liquid phase to aid dissolution of the M'_{ss} phase may be a factor which facilitates the M'_{ss} destabilisation.

High-Ca Sm–Ca-containing samples produce a Ca-rich $(M'\text{-}G)_{ss}$ grain boundary phase at 1300 °C, and in quantities comparable to that formed during the 1450 °C heat treatment. There is still the tendency for the amount of grain boundary phase to decrease with increasing calcium-for-samarium substitution, as observed after the 1450 °C heat treatments. It should be noted that gehlenite may be formed at this temperature in α′-containing regions in the Ca–Si–Al–O–N system.[11,26,27] Therefore, these results appear to indicate that the incorporation of more calcium into a Sm–Ca–Si–Al–O–N system gradually lowers the minimum $(M'\text{-}G)_{ss}$ phase formation temperature, until $(M'\text{-}G)_{ss}$ becomes the stable devitrification product at 1300 °C at some point between 40 eq% and 60 eq% calcium on a (Sm + Ca) basis.

Heat treatment (1300 °C) of the S8C2 and S6C4 samples has produced a Sm–Ca apatite phase, of approximate composition $Ca_2Sm_8(SiO_4)_6O_2$. The exact composition of this phase is uncertain, as it has been found in the Nd–Ca system that a solid solution of type $Ca_{2+x}Nd_{8-x}(SiO_4)_6O_{2-0.5x}$ may form, with a solubility limit of $x \sim 0.2$.[28] It is possible that such a solid solution will form in the Sm–Ca system as well. This apatite phase occurred in greater quantities in the mid-series S6C4 sample than in the high-Sm S8C2 sample, in which greater quantities of the $SmAlO_3$ phase were produced in the earlier stages of the 1300 °C heat treatment, and persist throughout the 192 h of heat treatment at 1300 °C.

The fact that the Sm–Ca apatite phase occurs in the high-Sm S8C2 and mid-series S6C4 samples seems to indicate that partitioning of the samarium and calcium cations is occurring between the α¢ phase and the grain boundary phases. In the apatite phase, the atomic ratio of samarium to calcium is 4:1 (or approximately 4:1 if a Sm–Ca solid solution forms in the Sm–Ca–apatite phase). As the Sm–Ca-apatite is the only grain boundary phase present after 192 h heat treatment at 1300 °C in the S6C4 sample (in which the designed Sm:Ca molar ratio is 1:1), it seems to indicate that considerably more samarium is present at the grain boundaries than would be expected purely from the designed composition. In the high-Sm S8C2 sample, the Sm:Ca design ratio is 8:3, which is less than the 4:1 ratio found in the Sm–Ca apatite phase, but higher than that with the S6C4 composition. Consequently, more samarium would be expected to stay at the grain boundaries in the S8C2 sample than in the S6C4 sample. From the XRD spectra, this additional samarium is balanced by the presence of small quantities of samarium aluminate that are found in this sample.

3.2. EPMA analyses of samples

3.2.1. EPMA analyses of the α′ phase

Results from the EPMA examination of the α′ phase are presented in Fig. 3. Note that examination of the pure-Ca Ca10 sample by EPMA was impossible due to a lack of compositional contrast between the phases. The α′ phase was examined after 96 hours heat treatment at 1450 °C.

It can be seen that the *m* value (the number of Al–N bonds substituted for Si–N bonds in the α′ phase) appears to remain approximately constant with increasing calcium, though there is a drop in m-value in the Sm–Ca samples as compared with the pure-Sm sample. The *m*-value in the α′ phase in the pure-Sm Sm10 sample is

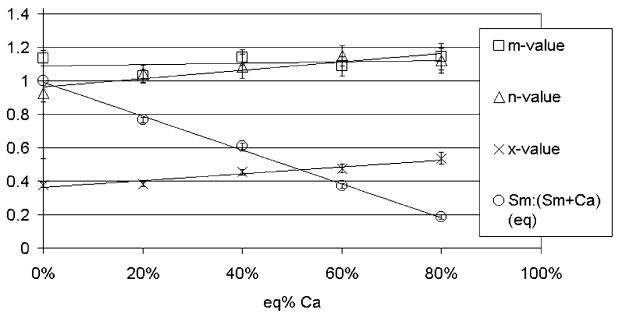

Fig. 3. The change in samarium-to-calcium equivalence ratio, *m*-, *n*- and *x*-values for the α-sialon phase, with increasing calcium content. In the design composition, the *m*-value is 1.194, and the *n*-value is 1.614.

1.13, fairly close to the design value of 1.194. The corresponding x-value increases with increasing calcium content in the sample, since more Ca^{2+} cations must be dissolved within the α' structure as compared with Sm^{3+} cations for the m-value to remain constant.

As may be expected from the unchanging m-value, the ratio of samarium to calcium in the α' phase appears to follow the design ratio reasonably closely, though several samples appear to exhibit a slight preference for calcium over samarium. There appears to be no great preference between the two cations in the α' phase in this system. However, it should be remembered from the XRD results that the stability of the α' phase has improved in the Ca-containing samples relative to the pure-Sm Sm10 sample. This indicates that the m-value of the α' phase (i.e. the equivalent content of α'-stabilising cations) is not the sole factor that controls its stability.

The n-value (the amount of Al–O bonds substituted for Si–N bonds in the α' phase) for the α' phase appears to increase with increasing calcium levels, and is significantly lower than the design value in all samples. This divergence is particularly significant in the pure-Sm sample, in which the n-value was determined to be just over half of the designed value of 1.614. Given that the m-value does not change significantly in this series, the increasing n-value with increasing calcium content seems to indicate that Al–O for Si–N substitution may play an important role in determining α' phase stability, and that this is controlled in part by the α'-stabilising cation used.

3.2.2. EPMA analyses of the M'_{ss}-Gehlenite phases

Results from the EPMA examination of the M'_{ss}-gehlenite phases are presented in Figs. 4–6. This phase was analysed after 96 h heat treatment at 1450 °C in all samples. The formula for the M'_{ss}-gehlenite solid solution in the Sm–Ca–Si–Al–O–N system is given as $Sm_{(2-z)}Ca_zSi_{3-x}Al_xO_{3+z+x}N_{4-z-x}$. Therefore, x-value denotes Al–O for Si–N substitution, and z-value denotes calcium-for-samarium substitution, with $0 \leqslant x \leqslant 3$ and $0 \leqslant z \leqslant 2$.

The M'_{ss} formula for the pure-Sm M'_{ss} produced in these series is found to be $Sm_2Si_{2.4}Al_{0.6}O_{3.6}N_{3.4}$ for the Sm10 sample, i.e. the base x-value for this composition is 0.6. Fig. 4 shows that the addition of calcium is found to correlate with an increase in aluminium content in the $(M'\text{-}G)_{ss}$ phase. This is unsurprising given that gehlenite is the preferred devitrification product in the α'-forming region of the Ca–Si–Al–O–N system under this heat treatment regime.[11,27] Compared with M'_{ss}, the gehlenite phase contains divalent calcium rather than a rare earth cation, and also has no nitrogen content. Therefore, gehlenite must contain considerably more aluminium than a corresponding M'_{ss} phase, and for a Ca-containing M'_{ss}-type phase to form the aluminium content would be expected to increase with increasing calcium in the composition.

The secondary α'-stabilising cation was found to be soluble in the M'_{ss} phase, as shown by an increase in z-value with increasing secondary cation content. The z-value for all samples is shown in Fig. 5, along with the designed z-value. By comparing the measured z-values (solid line in Fig. 5) with the designed z-values (dashed line), it can be seen that in all samples there is a definite preference for Sm over Ca in the M'_{ss} phase.

As noted earlier, there appears to be a correlation between x- and z-values in the M'_{ss} phase. x-Values for the $(M'\text{-}G)_{ss}$ phase are plotted against the z-value in Fig. 6, along with the x- and z- values of a pure-Ca gehlenite phase. These show that the M'_{ss} composition is

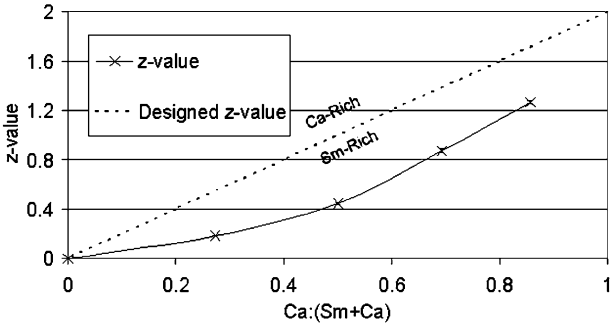

Fig. 5. The change in z-value for the melilite phase after 96 h heat treatment at 1450 °C, with increasing calcium content. The design z-value is shown by the dashed line.

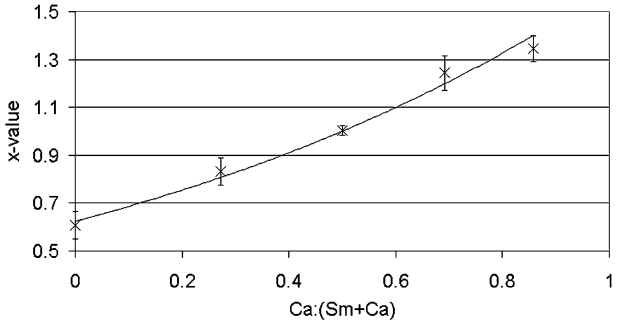

Fig. 4. The change in x-value for the melilite phase after 96 h heat treatment at 1450 °C, shown with increasing calcium content.

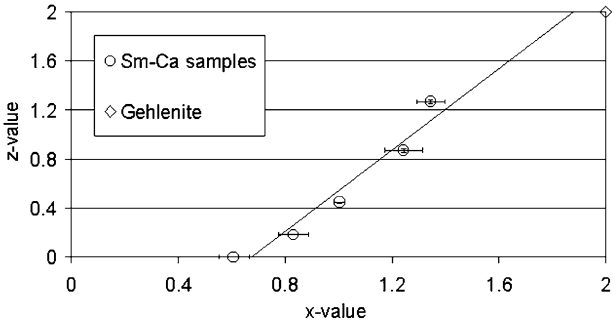

Fig. 6. x-Value plotted against z-value for the M'_{ss} phases, along with those for Gehlenite, $Ca_2SiAl_2O_7$.

moving towards that of gehlenite, with increasing calcium and aluminium solubility observed in the $(M¢\text{-}G)_{ss}$ phase with increasing calcium content.

3.3. Microstructural examination

3.3.1. Microstructural examination of as-fired samples

Fig. 7 shows the as-fired microstructures of the pure-Sm Sm10 sample, the mid-series S6C4 sample, the high-Ca S2C8 sample and the pure-Ca Ca10 sample. The microstructures of the Sm-containing samples are all shown using compositional backscattered electron contrast, whereas the pure Ca sample has been etched in molten NaOH, then coated in gold and imaged using secondary electrons.

Examination of the micrographs in Fig. 7 shows that the addition of calcium has resulted in the elongation of the α' grains, most significantly in the pure-Ca Ca10 sample but also visible in the mid-series S6C4 sample. It can also be seen that in the initial stages of calcium substitution, grain boundary glass levels remain approximately constant [Fig. 7(a) and (b)], but that as calcium becomes the predominant α'-stabilising cation, there is a gradual decrease in glass content. It may be argued that this apparent reduction in glass content is not real, and that it might be due to the reduction in contrast between the grain boundary glass and the α' phase as more samarium is replaced by calcium. However, it is believed that there is a genuine reduction, as despite the reduction in contrast, the grain boundary glass can still be seen in Fig. 7(c). This reduction in grain boundary glass content can be explained in terms of the compositional balance observed after heat treatment at 1450 °C, as the *m*- and *n*-values of a Ca-rich α' phase are closer to the design composition ($m = 1.194$, $n = 1.614$) than those found in a Sm-rich α' phase, as seen in Fig. 3. Therefore, a greater proportion of the $\alpha¢$ phase will be formed in a Ca-rich system than in a Sm-rich system, and the quantity of the $(M'\text{-}G)_{ss}$ phase subsequently formed in such Ca-rich systems by devitrification of the glass during heat treatment at 1450 °C will also be reduced. Thermodynamically, this translates to calcium being a better stabiliser of the α' phase than samarium, the latter allowing greater quantities of the grain boundary liquid phase to be produced.

Such a reduction in grain boundary liquid content is supported by measurement of the bulk densities in these samples. The bulk densities for all samples are shown in Fig. 8, with increasing calcium content. It can be seen that sample density reaches a maximum towards the middle of the series at the S6C4 sample. This would be related to both the viscosity and amount of the grain boundary phase. As calcium is introduced into the system, grain boundary glass viscosity would be expected to decrease. However, as discussed above, the grain boundary glass content is expected to decrease as calcium content

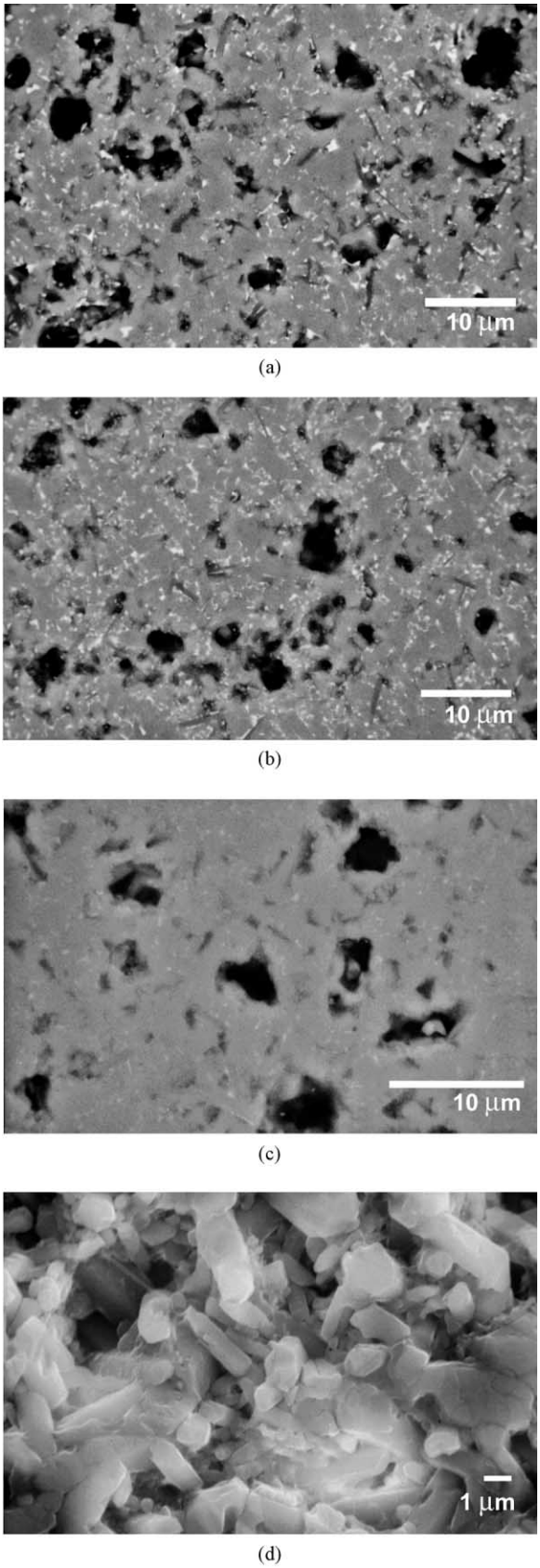

Fig. 7. The microstructures of selected as-sintered samples: (a) Sm10; (b) S6C4; (c) S2C8; (d) Ca10.

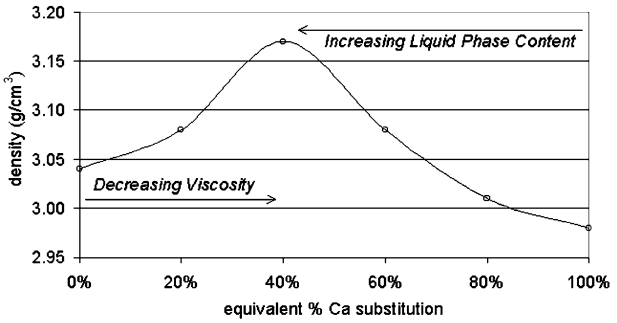

Fig. 8. The bulk densities of the different samples.

increases. Beyond the mid-series S6C4 sample, the assistance to densification from the reduction in grain boundary glass viscosity is outweighed by the reduced amount of that glass, so sample density reaches a maximum in the middle of the series. If grain boundary glass content did not decrease, the final density would be expected to be high in the high-calcium samples.

3.3.2. Microstructural examination of selected samples after heat treatment at 1450 °C

Figs. 9–11 show the microstructures of the pure-Sm Sm10 sample, the mid-series S6C4 sample and the high-Ca S2C8 sample after heat treatment at 1450 °C for 192 h. Segregation of the M'_{ss} phase into large clusters is apparent in the pure-Sm Sm10 sample, as seen in Fig. 9. It has been shown[29] that these clusters are often large single grains that have grown between prior α′ grains. M'_{ss}-poor regions seem to contain greater amounts of the β′ phase, whereas β′ content is suppressed in the immediate vicinity of the M'_{ss} clusters. This segregation of the M'_{ss} phase is less apparent in the mid-series S6C4 sample (Fig. 10), although there do appear to be some M'_{ss}-rich areas. Very little grain boundary phase can be seen in the high-calcium S2C8 sample, where the M'_{ss} grain size is also reduced, as shown in Fig. 11.

The M'_{ss} grain segregation may be explained as follows. The phase assemblage in these sialon systems, as achieved at the sintering temperature (1820 °C) may become unstable during post-sintering heat-treatment, and will generally proceed to a new equilibrium at a relatively slow rate A significant example of such a process is marked by the α′ phase decomposition to β′ and other phases in the Sm-sialon system, such as M'_{ss} and 21R [25]. As the β′ grains grow during the α′→β′ transformation, the α′-stabilising cations will move towards the grain boundary phase, for example, the $(M'\text{-}G)_{ss}$, depleting the region around the β′ grains of these cations, which further aids α′ decomposition and growth of the β′-rich regions. As α′-stabilising cations move towards the M'_{ss} grains, the regions through which they pass become α′-stabilising cation enriched, reducing the driving force for α′ phase decomposition. This process would naturally result in α′-poor/M'_{ss}-poor/β′-rich regions, which would grow as the α′ decomposition proceeds, and α′-rich/M'_{ss}-rich/β′-poor regions, which would gradually lose α′ phase as the M'_{ss} phase continues to grow. This observed microstructure also supports the belief that β′ phase formation preferentially

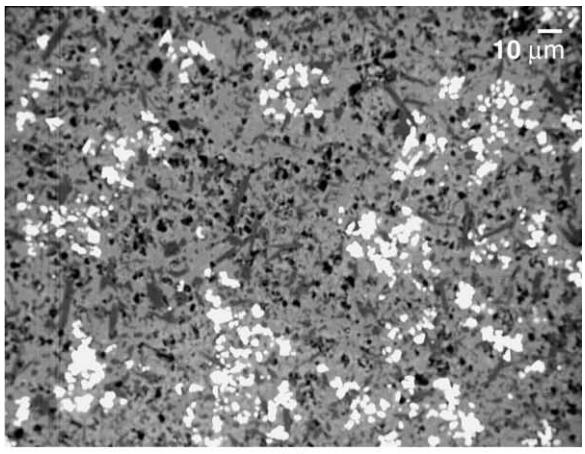

(a)

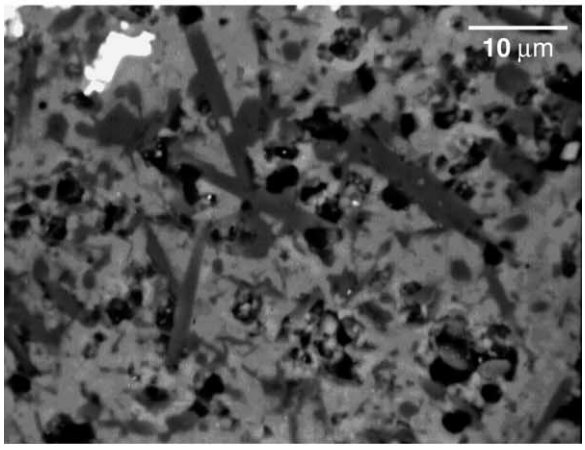

(b)

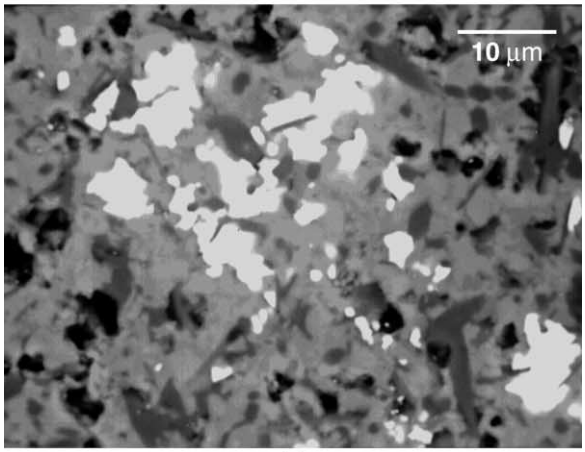

(c)

Fig. 9. The pure-Sm Sm10 sample after 192 h heat treatment at 1450 °C: (a) low magnification; (b) high magnification of β′-rich region; (c) high magnification of M'_{ss}-rich region.

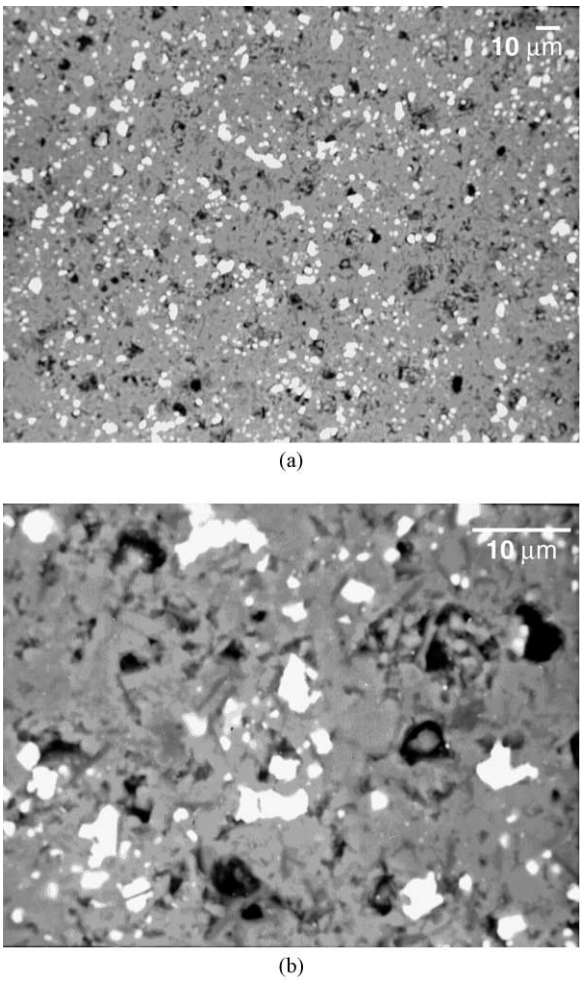

Fig. 10. The mid-series S6C4 sample after 192 h heat treatment at 1450 °C: (a) low magnification; (b) high magnification.

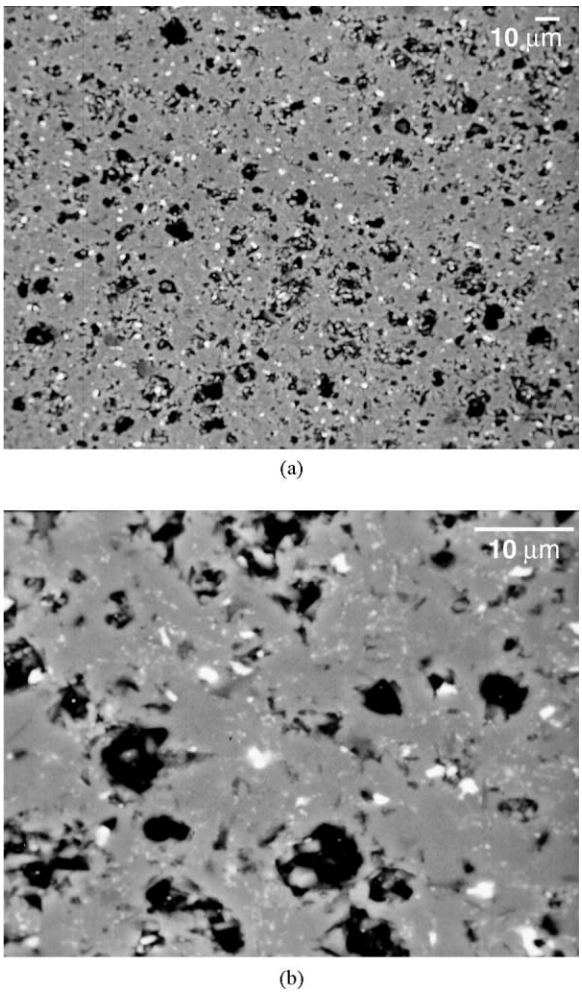

Fig. 11. The high-calcium S2C8 sample after 192 h heat treatment at 1450 °C: (a) low magnification; (b) high magnification.

takes place via the decomposition of the α′ grains and growth of prior β′ grains. This segregation would not be expected to occur if the α′ grains were able to transform to β′ directly, as the β′ grains could then be more evenly distributed throughout the microstructure. Where the α′ phase is stable, M'_{ss} formation will only be due to grain boundary glass devitrification, which will occur simultaneously throughout the system, resulting in a more even distribution of the M'_{ss} phase, as shown in Figs. 10 and 11. It is also worth noting the presence of M'_{ss} in the as-sintered pure-Sm Sm10 sample. The possibility for growth of M'_{ss} during post-sintering heat treatment onto these few prior grains may also enhance this tendency towards segregation of the M'_{ss} phase. Since $(M'\text{-}G)_{ss}$ was not present prior to heat treatment in the calcium-containing samples, $(M'\text{-}G)_{ss}$ grains must nucleate before growth, which would make $(M'\text{-}G)_{ss}$ formation more likely to occur throughout the microstructure rather than in small pockets.

Image analysis of these samples allows for an estimation of M'_{ss} phase content, and an estimation of the normalisation constants for the Sm–Ca containing M'_{ss} phases. Total M'_{ss} content for all of the samples is shown in Fig. 12. It can be seen that there is a general decrease in M'_{ss} phase content with increasing calcium content, more pronounced at higher calcium levels. The M'_{ss} content of the pure-Sm Sm10 sample continues to increase with increasing heat treatment time, as the $\alpha \rightarrow \beta'$ phase transformation takes place. After the initial heat treatment, the changes in $(M'\text{-}G)_{ss}$ content in all

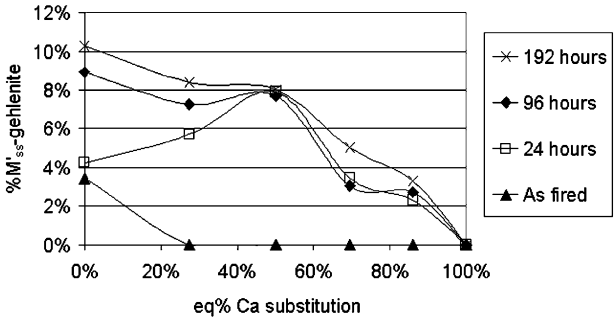

Fig. 12. The percentage of the $(M'\text{-}G)_{ss}$ phase prior to and after heat treatments at various conditions. Normalisation constants for the $(M'\text{-}G)_{ss}$ phases are estimated using image analysis techniques.

other samples are less pronounced, as $(M'\text{-}G)_{ss}$ formation in these samples comes solely from the devitrification of the grain boundary glass.

3.3.3. Microstructural examination of the samples after heat treatment at 1300 °C

Fig. 13 shows the microstructures of the pure-Sm Sm10 sample, the mid-series S6C4 sample and the high-Ca S2C8 sample after heat treatment at 1300 °C for 192 h. It can be seen that grain boundary phase content does not differ greatly from the high-Sm samples towards the middle of the series, followed by a decrease once calcium becomes the predominant α′-stabilising cation. The $SmAlO_3$ and Sm–Ca–apatite phases are both seen to be evenly distributed throughout the microstructure and fine-grained when compared with the M'_{ss} phase that occurs in these samples after a 1450 °C heat treatment. It should be noted that phase development is slower during the 1300 °C heat treatment than at 1450 °C, as diffusion would be considerably slower due to the lower kinetic energy and higher viscosity of the grain boundary glass. This can be seen from a comparison of XRD peak intensities in Table 2 between the M'_{ss} and the $SmAlO_3$ and apatite phases at comparable stages of their respective 1450 and 1300 °C heat treatments. When the most intense peaks for the $(M'\text{-}G)_{ss}$, $SmAlO_3$ and apatite phases are compared, the $SmAlO_3$ and apatite peaks are generally lower in intensity than the comparable $(M'\text{-}G)_{ss}$ peak. This is despite the fact that calculated structure factors for these three peaks are comparable[21] ($F_{211} = 143.94$ for a Sm–M'_{ss}, $F_{211} = 148.65$ for Sm–Ca–apatite, $\Sigma(F_{200} + F_{020}) = 123.47$ for $SmAlO_3$). Furthermore, the relative intensity of the stronger peaks from the smaller-grained phases produced during grain boundary devitrification at 1300 °C should also be less affected by primary extinction relative to comparable peaks from their large-grained $(M'\text{-}G)_{ss}$ counterparts,[22] Therefore, phase development is a much more localised phenomenon in all of these samples under a 1300 °C heat treatment than at 1450 °C, leading to a greater number of smaller grains of the devitrification product.

4. Discussion

In terms of grain boundary phase evolution, the M'_{ss} phase evolution, and the evolution of Sm-rich $(M'\text{-}G)_{ss}$ phases were the most striking in these series. M'_{ss} formation on heat treatment was rapid and produced large M'_{ss} grains segregated throughout the microstructure, with large β′-rich clusters simultaneously forming away from the M'_{ss} phase. M'_{ss} formation has been noted before for its rapidity during 1450 °C heat treatment in Sm- and Nd-sialon systems.[23,25,30,31] M'_{ss} may be a more stable phase relative to the α′ phase at this heat treatment temperature, resulting in the observed rapid growth of the M'_{ss} phase and decomposition of the α′ phase. As more calcium is introduced into these systems, $(M'\text{-}G)_{ss}$ is formed, and the $(M'\text{-}G)_{ss}$ composition moves further towards that of gehlenite, which may be relatively more compatible with the α′ phase.

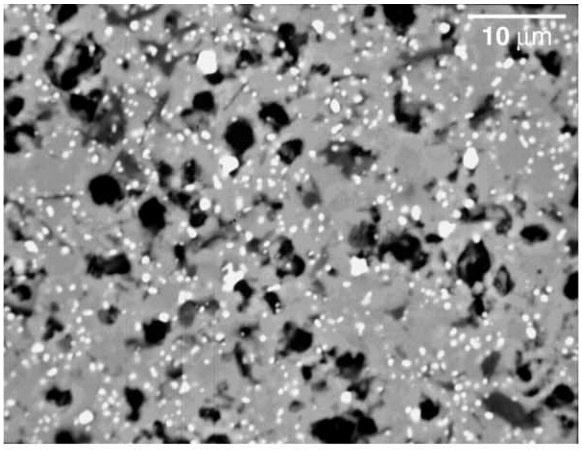

(a)

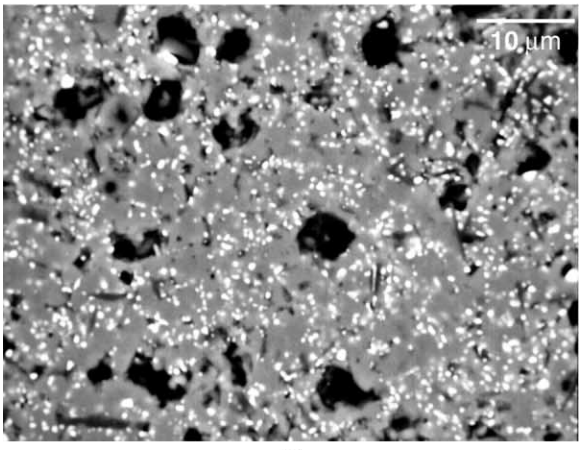

(b)

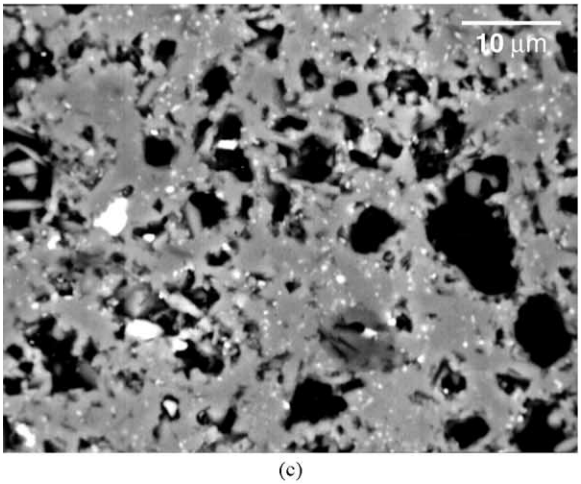

(c)

Fig. 13. The microstructures of selected samples after 192 h heat-treatment at 1300 °C: (a) Sm10; (b) S6C4; (c) S2C8.

One possible advantage of choosing seemingly incompatible cations is that new or unexpected grain boundary phases may arise, such as the apatite phases found. Apatites have been found before in Nd–Si–O–N and Y–Si–O–N systems,[32] and used as a grain boundary phase for Si_3N_4,[33–36] often in multi-component systems, such as $MgO–Nd_2O_3$.[33–35] Apatite phases have also been found in equilibrium with the β-sialon phase,[32] and the M'_{ss} phase,[37] but never in equilibrium with the α-sialon phase in sialon systems containing a single α-stabilising-cation. Redington and Hampshire[38] have found a Nd-containing apatite in the Nd–Li-sialon system after sintering, but reported this as a Li-free Nd–N–apatite of composition $Nd_{10}(SiO_4)_6N_2$, and have not examined such a system after heat treatment.

Grain boundary phase evolution in these samples is faster and less complex at 1450 °C than at 1300 °C. Only one grain boundary phase is generally observed on heat treatment at 1450 °C—namely, the M'_{ss} or $(M'\text{-}G)_{ss}$ phase- and may be observed to form in small pockets throughout the microstructure, rather than being evenly dispersed. While both calcium and samarium are soluble within the apatite phase found in these series, the range of solubility is quite limited, especially when compared with the apparently continuous solid solution that forms between melilite and gehlenite.

5. Conclusions

- Incorporation of a secondary α′-stabilising cation on a substitutional basis can improve the stability of the α′ phase, where the secondary α′-stabilising cation is a better α′-stabiliser than the first.
- Incorporation of a secondary cation on a substitutional basis does not result in an increase in grain boundary glass content, and will generally result in a decrease in glass content and sample density, where the secondary cation is a better α′-forming additive than the primary cation.
- Depending on the ratio and type of α′ stabilising additives used, new grain boundary phases may be produced, such as the apatite-type phases formed in some of these samples after heat treatment at 1300 °C.
- The M'_{ss} phase is unstable at 1300 °C, and will dissolve into the grain boundary glass to produce the $SmAlO_3$ phase.

References

1. Hampshire, S., Park, H. K., Thompson, D. P. and Jack, K. H., α′-Sialon ceramics. *Nature*, 1978, **274**, 880–882.
2. Jack, K. H., The characterisation of α′-sialons and the α–β relationships in sialons and silicon nitrides. In *Progress in Nitrogen Ceramics*, ed. F. L. Riley. Martinus Nijhoff, 1983. p. 45–60.
3. Chen, I. W. and Rosenflanz, A., A tough SiAlON ceramic based on α-Si_3N_4 with a whisker-like microstructure. *Nature*, 1997, **389**(16 October), 701–704.
4. Wood, C. A. and Cheng, Y.-B., Phase relationships and microstructures of Ca and Al-rich α-sialon ceramics. *J. Eur. Ceram. Soc.*, 2000, **20**, 357–366.
5. Mandal, H., Thompson, D. P. and Ekstrom, T., Reversible α↔β sialon transformation in heat-treated sialon ceramics. *J. Eur. Ceram. Soc.*, 1993, **12**, 421–429.
6. Mandal, H., Thompson, D. P., Sun, W. Y. and Ekstrom, T., Mechanical property control of rare earth oxide densified α-β sialon composites by α↔β sialon transformation. In *5th International Symposium on Ceramic Materials and Components for Engines*. World Scientific, Singapore, 1994.
7. Shen, Z., Ekstrom, T. and Nygren, M., Reactions occurring in post heat treated α/β sialons: on the thermal stability of α-sialon. *J. Eur. Ceram. Soc.*, 1996, **16**, 873–883.
8. Camuscu, N., Thompson, D. P. and Mandal, H., Effect of starting composition, type of rare earth sintering additive and amount of liquid phase on α↔β sialon transformation. *J. Eur. Ceram. Soc.*, 1997, **17**, 599–613.
9. Mandal, H. and Thompson, D. P., Preparation and characteristics of glass-free silicon nitride ceramics. In *Fourth Conference of the European Ceramic Society. 1994*. Gruppo Editoriale Faentza, Italy, 1997, pp. 287–294.
10. Messier, D. R., Riley, F. L. and Brook, R. J., The α/β silicon nitride phase transformation. *J. Mater. Sci.*, 1978, **13**, 1199–1205.
11. Hewett, C. L., Cheng, Y.-B., Muddle, B. C. and Trigg, M. B., Thermal stability of calcium α-sialon ceramics. *J. Eur. Ceram. Soc.*, 1998, **18**, 417–427.
12. Mandal, H. and Thompson, D. P., α→β Sialon transformation in calcium-containing α-sialon ceramics. *J. Eur. Ceram. Soc.*, 1999, **19**, 543–552.
13. Cheng, Y.-B. and Thompson, D. P., Preparation and grain boundary devitrification of samarium α-sialon ceramics. *J. Eur. Ceram. Soc.*, 1994, **14**, 13–21.
14. Ekstrom, T., Jannson, K., Olsson, P. O. and Persson, J., Formation of an Y/Ce-doped α-sialon phase. *J. Eur. Ceram. Soc.*, 1991, **8**, 3–9.
15. Hwang, C. J., Susnitszky, D. W. and Beaman, D. R., Preparation of multication α-sialon containing strontium. *J. Am. Ceram. Soc.*, 1995, **78**(3), 588–592.
16. Mandal, H. and Hoffmann, M. J., Preparation of multiple-cation α-sialon ceramics containing lanthanum. *J. Am. Ceram. Soc.*, 1999, **82**(1), 229–232.
17. Chen, W. W., Sun, W. Y., Li, Y. W. and Yan, D. S., Microstructure of (Y + Sm)-α-sialon with α-sialon seeds. *J. Mater. Res.*, 2000, **15**(10), 2223–2227.
18. Mandal, H., Oberacker, R., Hoffmann, M. J. and Thompson, D. P., α-Sialon Ceramics Densified with Mixed Oxide Sintering Additives, *Mat. Sci. Forum*, 2000, **325–326**, 207–212.
19. Gazzara, C. P. and Messier, D. R., Determination of phase content of Si_3N_4 by x-ray diffraction analysis. *Ceram. Bull.*, 1977, **56**(9), 777–780.
20. Li, D. Y., O'Connor, B. H., Chen, Q. T. and Zadnik, M. G., Quantitative powder X-ray diffractometry phase analysis of silicon nitride materials by a multiline, mean-normalized-intensity method. *J. Am. Ceram. Soc.*, 1994, **77**(8), 2195–2198.
21. Payne, J., *Volfract*. 1992.
22. Cullity, B. D., Elements of X-ray Diffraction, 2nd ed., Addison-Wesley Publishing Company, Reading, Mass, 1978.
23. Sun, W. Y., Wang, P. L. and Yan, D. S., Phase transformation in Ln-(α + β)-sialon ceramics by heat treatment. *Mater. Lett.*, 1996, **26**, 9–16.
24. Sun, W. Y. *et al.*, Subsolidus phase relationships in the systems $Ln_2O_3–Si_3N_4–AlN–Al_2O_3$ (Ln = Nd, Sm). *J. Eur. Ceram. Soc.*, 1995, **15**, 349–355.

25. Zhao, R. and Cheng, Y.-B., Decomposition of Sm α-sialon phases during post-sintering heat treatment. *J. Eur. Ceram. Soc.*, 1996, **16**, 1001–1008.
26. Hewett, C. L., Cheng, Y.-B., Muddle, B. C. and Trigg, M. B., Reaction mechanism of hot-pressed calcium α-SiAlON. In *Aust-ceram 94*. 1994, International Ceramic Monographs, 1001–1006.
27. van Rutten, J. W. T., Hintzen, H. T. and Metselaar, R., Phase formation of Ca-α-sialon by reaction sintering. *J. Eur. Ceram. Soc.*, 1996, **16**, 995–999.
28. Fahey, J. A., Weber, W. J. and Rotella, F. J., An X-ray and neutron powder diffraction study of the $Ca_{2+x}Nd_{8-x}(SiO_4)_6O_{2-0.5x}$ system. *J. Solid State Chem.*, 1985, **60**, 145–158.
29. Swenser, S. 1998, Private communication.
30. Shen, Z. J., Ashkin, D., Babushkin, O. and Ekstrom, T., Melilite formation in a samarium-stabilised α-sialon ceramic during post-sintering heat treatments. *J. Am. Ceram. Soc.*, 1997, **80**(3), 817–821.
31. Mandal, H., Camuscu, N. and Thompson, D. P., Comparison of the effectiveness of rare-earth sintering additives on the high-temperature stability of α-sialon ceramics. *J. Mater. Sci.*, 1995, **30**, 5901–5909.
32. Slasor, S., Liddell, K. and Thompson, D. P., The role of Nd_2O_3 as an additive in the formation of α′ and β′ sialons. *Br. Ceram. Proc.*, 1986, **37**, 51–64.
33. Saruhan, B., Pomeroy, M. J. and Hampshire, S., Microstructural development and secondary phases in silicon nitride sintered with mixed neodymia/magnesia additions. In *Non-oxide, Technical and Engineering Ceramics*. Elsevier, 1986. pp. 69–82.
34. Hampshire, S. *et al.*, Crystallisation heat treatments of silicon nitride ceramics and glass-ceramics containing neodymia. In *3rd International Symposium on Ceramic Materials and Components for Engines*. 1988, Las Vegas, NV, USA, American Ceramic Society Incorporated, pp. 432–442.
35. Patel, J. K. and Thompson, D. P., The devitrification behaviour of grain boundary glasses in silicon nitride densified with mixed magnesia, yttria additions. *Br. Ceram. Proc.*, 1992, **39**, 61–68.
36. Tiegs, T. N., *et al.*, Fabrication and properties of Si_3N_4 with rare-earth apatite grain boundary phases. *Mater. Res. Soc. Symp. Proc.*, 1993, **287**, 353–358.
37. Chee, K. S., Cheng, Y.-B. and Smith, M. E., The solubility of aluminium in rare earth nitrogen melilite phases. *J. Eur. Ceram. Soc.*, 1995, **15**, 1213–1220.
38. Redington, M. and Hampshire, S., Multi-cation α-sialons. *Br. Ceram. Proc.*, 1992, **49**, 175–190.